Anisotropic mechanical response of a 2D covalently bound fullerene lattice

Shuai Zhao [a,b], Xibei Zhang [a,c], Yong Ni [b], Qing Peng [a,c,**], Yujie Wei [a,c,*]

[a] *State Key Laboratory of Nonlinear Mechanics (LNM), Institute of Mechanics, Chinese Academy of Sciences, Beijing, 100190, China*
[b] *Department of Modern Mechanics, University of Science and Technology of China, Hefei, Anhui, 230026, China*
[c] *School of Engineering Sciences, University of Chinese Academy of Sciences, Beijing, 100049, China*

ARTICLE INFO

ABSTRACT

Contrary to the monotype intercell connection in a hexagonal structure material, newly synthesized stable monolayer C_{60} fullerene (mC_{60}) lattice possesses two kinds of intercell connection, and anisotropic properties are thus expected. Herein, we have investigated the anisotropy mechanical properties of the mC_{60} using first-principles calculations within the framework of density functional theory (DFT) and theoretical analysis. Uniaxial tensile properties of mC_{60} are orientation-dependent, and the ultimate tensile strength and the work-to-fracture of mC_{60} reach their maxima at $15°$ and minima at $75°$, respectively. A theoretical expression, based on strain-governed bond failure criterion, has been developed for the strength-loading direction relationship of mC_{60}. The theory captures well with the orientation-dependent strength from DFT calculations. We further illustrate that mC_{60}'s band gap may be largely tuned through strain engineering. Our atomistic insights and the theoretical on the structure – mechanical property relationship might be helpful in the exploring of the functioning and application of mC_{60}, which may be further generalized to the mechanical analysis of other monolayer lattices.

1. Introduction

Owning to the quantum confinement, low dimensional materials possess unique properties compared to their bulk counterparts [1,2]. Since the first successful preparation of graphene [3–9], a new world of two-dimensional materials comes [10–12]. Thousands of two-dimensional materials emerged, including boronitrene [13], stanene [14], MoS_2 [15], graphyne [16,17], monolayer amorphous carbon [18], and many others. 2D nanostructures have an important impact on a variety of applications, from high-performance sensors and electronic devices to gas separation or storage, catalysis, inert coatings and supporting membranes [7,19–22]. So far most two-dimensional materials are limited to periodic network structures interwoven by monatomic structural units.

Recently, Hou, et al. have synthesized a single crystal 2D carbon material, namely monolayer quasi-hexagonal phase fullerene (denoted as mC_{60} hereafter) [23]. In this monolayer polymer, the cluster cages of C_{60} are covalently bonded to each other in a plane. Different from other hexagonal structures, there are two kinds of inter-cell connections: one is the common single C–C bond and the other is the [2 + 2]

cycloaddition bond (denoted as D-bond hereafter). The measurement of electron band structure shows that the transport band gap is about 1.6 eV mC_{60} has high crystallinity, good thermodynamic stability, significant in-plane anisotropy, including anisotropic phonon modes and conductivity. This kind of two-dimensional carbon material with medium band gap and unique topology provides an interesting platform for the potential applications of two-dimensional electronic devices.

A reliable structure property relationship in two-dimensional crystals is crucial for material design and promising applications [24–26]. Stability, integrity and mechanics are not only of great significance to related engineering applications, but also play an important role in understanding the unique properties of this new topological structure [27]. Tromer et al. [28] have investigated the electronic and mechanical properties of mC_{60} using GGA-PBE based on DFT simulations. They explored the mechanical properties of mC_{60} under uniaxial tension along two directions only.

Despite efforts, the angle dependent tensile properties are missing. Because there are two distinct inter-cell connections, property anisotropy is expected but still elusive. In addition, there is a lack of theory for this newly monolayer C60 fullerene lattice. Motivated by these gaps, we

have systematically investigated the thermal stability, anisotropic elastic and tensile properties of mC$_{60}$ using first-principles calculations and molecular dynamics simulations. Phonon spectrum has been calculated and its thermal stability is tested. The ultimate tensile strength, tensile toughness, and elastic constants have been examined. We have developed an elastic theory to capture the strongly orientation-dependent strength in mC$_{60}$. The electronic band structure and density of states are calculated and compared with the experimental values in the literature [23]. Further exploration indicates strain engineering could be applied to tune the band gap of mC$_{60}$.

2. Simulation method

The primitive cell of 2D mC$_{60}$ contains 60 carbon atoms. The vacuum space is fixed at 13 Å to avoid spurious interactions with periodic images of the structure. Vienna ab initio simulation package (VASP) [29] was used to implement first principles calculations based on the density functional theory (DFT) method where the interactions between ions and valence electrons were described by the projector augmented wave (PAW) pseudopotential [30]. Semi-local functional the Perdew-Burke-Ernzerhof (PBE) parameterization for the generalized gradient approximation (GGA) [31] was used in the calculations of the ground state of DFT except the hybrid functional for electronic band structure. For the primitive cell, a gamma-centered Monkhorst-Pack [32] grid of 4 × 4 × 1 was applied to integration sampling points in the first Brillouin zone, while a 2 × 2 × 1 k-point grid for the 2 × 2 × 1 supercells. The cutoff energy for plane wave was chosen as 520 eV. Electronic

self-consistent loop calculation stops once the total energy change to be smaller than 10^{-8} eV. Similarly, the force components convergence criteria were 10^{-3} eV/Å for structural optimization during the energy minimization by conjugate gradient (CG) method, and 10^{-4} eV/Å for those highly correlated with stability.

The ground state is obtained by relaxation of both atomic co-ordinates and supercell vectors simultaneously, except the z-axis vector for the latter. The van der Waals (vdW) dispersion correction has small effect on the electronic structures: the difference of lattice parameter is 0.49%, varying from 9.1916 Å (without vdW) to 9.1466 Å (with vdW) by using the method of DFT-D3 [33]. The second order interatomic force constants, phonon spectrum, thermal properties and phonon DOS are calculated by Phonopy [34] with a supercell of 2 × 2 × 1. In our uniaxial tensile tests, enforced small increment displacements along the tensile direction was employed one after another respect to the controlled Lagrange strain. Displacement was free along the direction in plane, perpendicular to the tensile one, and the atomic positions were opti-mized after each deformation to press on towards the quasi-static pro-cess. For the elastic constants calculations, six kinds of displacement corresponding to six components of strain matrix are applied respec-tively. Stress components were used after the ionic optimization, by Hook's law, to straightforward calculate the elastic constants. For band structure and density of states, both pure PBE exchange-correlation functional and a hybrid functional where a quarter of the short range of exchange part is replaced by Hartree-Fork correction [35] are applied respectively.
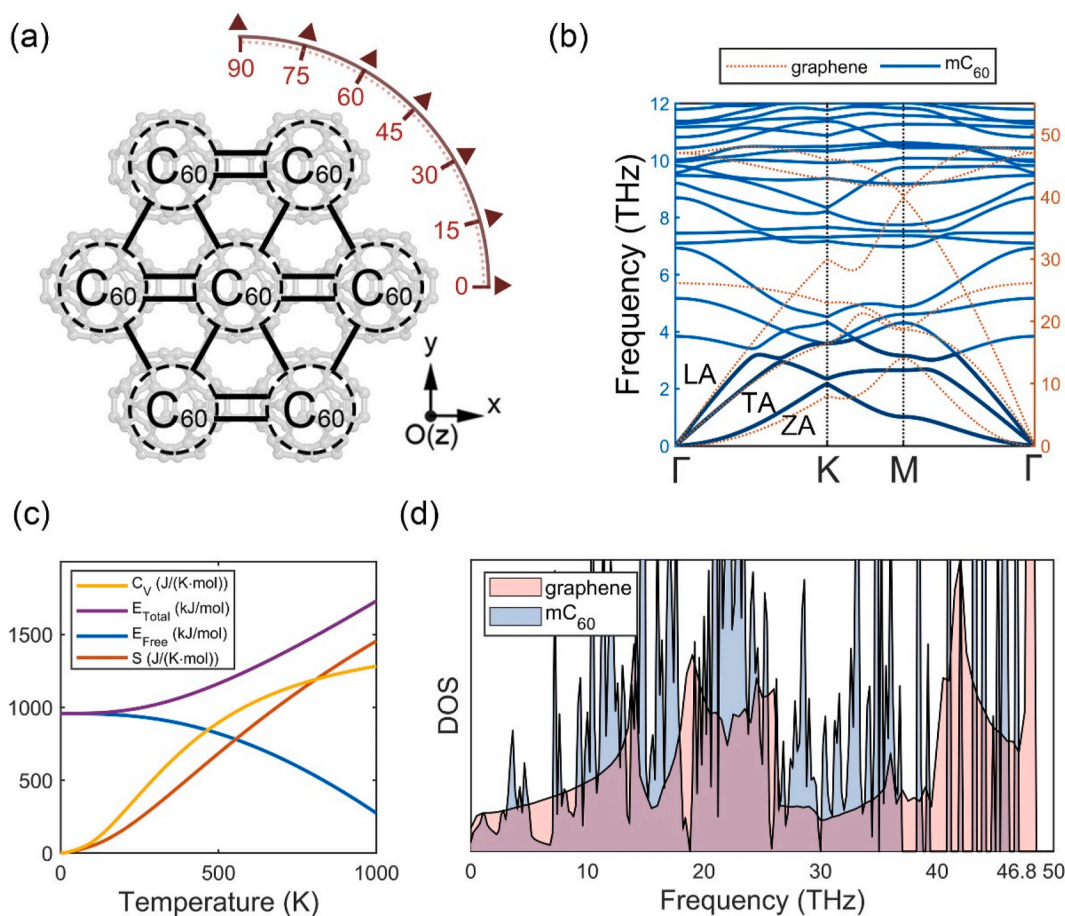

Fig. 1. Stability validation and thermal properties of mC60. (a) Projected view of mC$_{60}$ showing bond connections. The tensile directions are also shown. (b) Phonon band structure of mC$_{60}$ around the acoustic modes (solid blue lines) compared to that of monolayer graphene (dotted red lines). (c) Constant volume heat capacity C$_V$, total harmonic phonon energy E$_{Total}$, Helmholtz free energy E$_{Free}$ and entropy S as a function of temperature up to 1000 K. (d) Phonon density of states (DOS) of mC$_{60}$ (blue) and graphene (red). (A colour version of this figure can be viewed online.)

3. Results and discussion

Stability and integrity are the first-most concern for a new material. A projected view of the relaxed structure of mC_{60} is shown in Fig. 1(a). To examine the stability, the phonon dispersion has been calculated as presented in Fig. 1(b), compared with that of graphene. The band distribution is much denser due to the much larger primitive unit cell (60 atoms). There are three acoustic phonon modes and 177 optical phonon modes for mC_{60} while monolayer graphene has 6 in total. Thereby, merely the dispersion curves in the vicinity of the acoustic modes for mC_{60} is plotted for better view. The full phonon dispersion curves are displayed in Fig. S1 of the supplementary materials. The phonon dispersion curves of monolayer graphene are also displayed as a reference. These monolayer structures are strain-free without external pressure at the ground state. The absence of imaginary frequency declares its dynamical stability, in consistent with the success in experimental fabrication. Three acoustic branches, longitudinal acoustic (LA), transverse acoustic (TA) and flexural acoustic (ZA) modes, show the typical phonon disperse mode for 2D materials [36]. At the Γ point, ZA mode possesses a quadratic dependence on the wave vector, making it much flatter than the other two with a linear function of wave vector. It can be inferred that the phonon transport is more difficult from the much smaller slope because of the vacuum slab set to simulate the monolayer effect, and this ZA acoustic branch correspond to the flexural rigid translation mode.

With harmonic approximation, we have examined the thermal dynamics properties. The variations of thermal dynamics of constant volume heat capacity C_V, total harmonic phonon energy E_{Total}, Helmholtz free energy E_{Free} and entropy S under temperatures ranged from 0 to 1000 K are represented in Fig. 1(c). The Debye temperature is about 230 K, estimated by the average sound vector derived from the elastic constants, which is much lower than that (411 K) of the monolayer graphene. At a room temperature of 300 K, the constant volume heat capacity C_V, total harmonic phonon energy E_{Total}, Helmholtz free energy E_{Free} and entropy S are 522 J/(K·mol), 1019 kJ/mol, 922 kJ/mol, and 324 J/(K·mol), respectively.

The phonon density of states (DOS) for mC_{60} is plotted in Fig. 1(d), compared with that of graphene. The highest frequency, about 46.8 THz, can be read from the global phonon DOS, a value close to that of graphene, and is also in agreement with Raman spectrum observed from experiments [23]. DOS fluctuates with plenty of peaks, which is distinct from that of graphene. There are multiple band gaps occur between 37 THz and 45 THz in Fig. S2 of the supplementary materials. The propagation of elastic waves crossing these ranges is forbidden. As a consequence, the multiple phonon processing is limited and phonon anharmonicity is suppressed [37]. The elastic wave can be introduced within these band gaps through breaking the crystal periodicity by local defects.

The unique structure of mC_{60} with D bonds dictates the orientation-dependent mechanical properties in plane. We have examined the
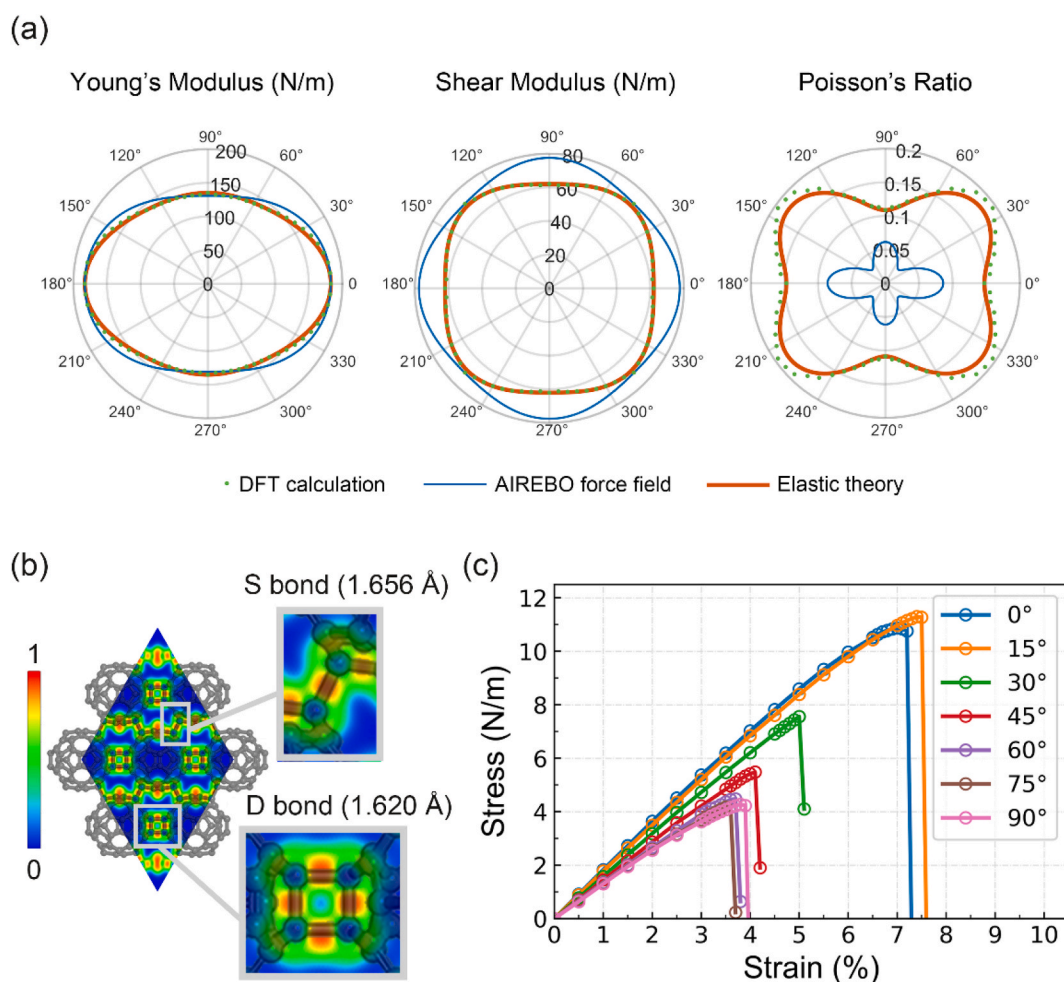

Fig. 2. Anisotropic mechanical properties of mC60. (a) Anisotropic elasticity: the Young's modulus, shear modulus and Poisson's ratio of mC_{60} in different orientations. As a comparison, data from three different methods are shown. (b) The ELF of optimized m mC_{60}. The difference of the two types of bonds can be clearly seen in the enlarged subgraphs. (c) Uniaxial stress–strain relations of mC_{60} in the seven directions using DFT calculations. (A colour version of this figure can be viewed online.)

elastic constants combinations every 5° in the first quadrant using first-principles calculations within the framework of density functional theory (DFT). The 2D Young's modulus E, 2D shear modulus G, and Poisson's ratio ν can be derived from the elastic constant combinations, as is shown in Fig. 2(a). Our first-principles study is self-consistent that Young's modulus has the same value with that derived from our uniaxial tensile tests, with the maximum value of 183 N/m along the direction of 0° and the minimum value of 133 N/m along that of 90°.

The theoretical elastic matrix C^{θ} can be calculated from the elastic constants C at $\theta = 0°$ using transformation matrix T_1 and T_2 of Voigt notation for stress σ and strain ε, respectively, whose form is given in Eqn. (1):

$$C^{\theta} = T_1^{-1} C_0 T_2 = \begin{bmatrix} \alpha^2 & \beta^2 & 2\alpha\beta \\ \beta^2 & \alpha^2 & -2\alpha\beta \\ -\alpha\beta & \alpha\beta & \alpha^2 - \beta^2 \end{bmatrix}^{-1} \begin{bmatrix} C_{11} & C_{12} & 0 \\ C_{12} & C_{22} & 0 \\ 0 & 0 & C_{66} \end{bmatrix} \begin{bmatrix} \alpha^2 & \beta^2 & \alpha\beta \\ \beta^2 & \alpha^2 & -\alpha\beta \\ -2\alpha\beta & 2\alpha\beta & \alpha^2 - \beta^2 \end{bmatrix}, \tag{1}$$

where $\alpha = \sin\theta$ and $\beta = \cos\theta$. Owing to the anisotropic connection, mC_{60} is of in-plane anisotropy. As one of the quadratic symmetry 2D materials [38], there are four independent elastic constants: C_{11}, C_{22}, C_{12} and C_{66}, which are 185.8, 137.3, 20.2 and 62.0 N/m, respectively. In general, the stiffness of graphene is around 340 N/m [4]. Our results are described well by the elastic formula in Eqn. (1), as seen in Fig. 2(a). We note that shear modulus doesn't exhibit strong anisotropic varying from 61.5 to 71.0 N/m, opposed to that of Poisson's ratio, ranging from 0.11 to 0.20.

Furthermore, we have investigated the mechanical properties at finite temperatures using molecular dynamics (MD) simulations with the AIREBO force field [39]. The predicted elastic constants are 183.8, 131.2, 11.3 and 77.5 N/m for C_{11}, C_{22}, C_{12} and C_{66}, respectively. In general, contrast with the results of DFT, the tensile prediction ability, highly correlated to C_{11} and C_{22}, is of high accuracy. However, the Poisson's effect, which is associated with C_{12}, is severely underestimated.

Besides, the bonding and electronic charge density distribution are examined via the electron location function (ELF) – a spatial function that describes the atomic bonding characteristics of structures – and shown in Fig. 2(b), which makes the difference of the two bonds more intuitively. The two typical bonds to form network of fullerene C_{60} are more clearly illustrated in Fig. 2(b) where dashed ball represents simplified C_{60}. Note in what follows we refer the connection with a single bond as S-bond, and that double connected as D-bond. To scrutinize the anisotropic mechanical properties of mC_{60}, uniaxial tensile tests along the seven directions are obtained by using first-principles calculations. Seven tensile orientations are illustrated in Fig. 1(a) and the C–C bond length is labeled in Fig. 2(b). The stress-strain curves along all are shown in Fig. 2(c). It is clear that mC_{60} is brittle in nature, as reflected by the sharp drop of the stress curves after reaching its peak.

As demonstrated in Fig. 3(a), mC_{60} many experience different failure modes: when D-bonds account for failure (Mode D), the strength is high, in contrast to the lower strength associated with S-bond breakage (Mode S); and mC_{60} reaches its highest strength if and only if both types of bond
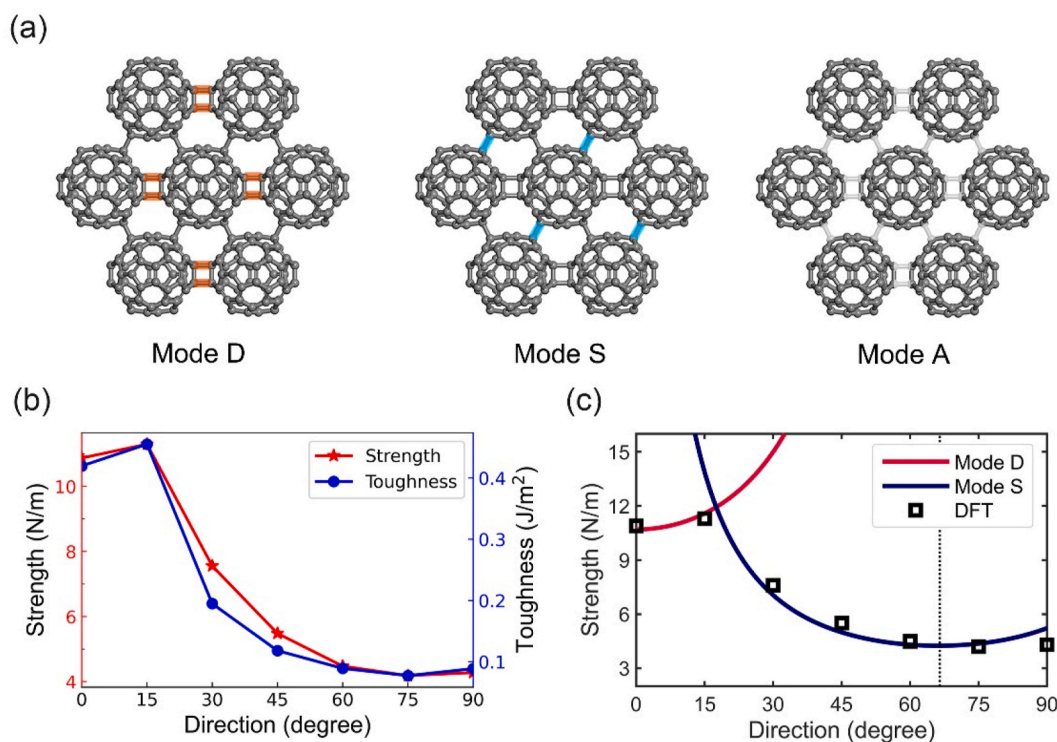

Fig. 3. Bond failure modes and orientation-dependent strength. (a) Three characteristic failure modes of mC_{60} under uniaxial tension: Mode D: initial failure in D-bonds, Mode S: S-bonds fail precede to others, and Mode A: all types of bonds fail simultaneously, corresponding to the highest strength of mC_{60}. (b) Ultimate tensile strength and work-to-fracture along the seven loading directions. (c) Theoretical predictions (lines) on the strength-orientation relationship and the critical stress to break the mC_{60} under different failure modes. (A colour version of this figure can be viewed online.)

may break simultaneously, as referred to Mode A. Therefore, mC_{60} has strong anisotropy in both ultimate tensile strength and work-to-fracture, as shown in Fig. 3(b). The work-to-fracture measures the resistance to the failure during tensile test, defined as the area under the stress-strain curve. The highest value of strength is about 11.3 N/m along the direction nearby 15°, and the lowest value is 4.2 N/m along the direction close to 75°.

To shed light on the strength anisotropy in mC_{60}, we consider a linear behavior between stress σ and strain ε given the brittle nature of mC_{60}, and have:

$$\{\varepsilon(\theta)\} = \left(C^\theta\right)^{-1}\{\sigma(\theta)\} = \begin{bmatrix} \varepsilon_1 \\ \varepsilon_2 \\ \gamma_{12} \end{bmatrix} = \left(C^\theta\right)^{-1}\begin{bmatrix} \sigma \\ 0 \\ 0 \end{bmatrix} = A\begin{bmatrix} B_1 \\ B_2 \\ B_3 \end{bmatrix}\sigma, \quad (2)$$

when mC_{60} is under stretch along θ direction (with respect to the x-axis defined in Fig. 1(a)). C_θ is the elastic stiffness tensor for mC_{60} in a co-ordinate with x-axis parallel to the stretch direction θ, as well as stress σ and strain ε, and is given in Eqn. (1). The coefficients A is given as

$$A = \frac{1}{|C^\theta|} = \left[2C_{12}^\theta C_{16}^\theta C_{26}^\theta + C_{11}^\theta C_{22}^\theta C_{66}^\theta - C_{22}^\theta \left(C_{16}^\theta\right)^2 - C_{11}^\theta \left(C_{26}^\theta\right)^2 - C_{12}^\theta \left(C_{66}^\theta\right)^2\right]^{-1}, \quad (3a)$$

and B_1, B_2 and B_3 are

$$B_1 = C_{22}^\theta C_{66}^\theta - \left(C_{26}^\theta\right)^2, B_2 = C_{16}^\theta C_{26}^\theta - C_{12}^\theta C_{66}^\theta, B_3 = C_{12}^\theta C_{26}^\theta - C_{16}^\theta C_{22}^\theta. \quad (3b)$$

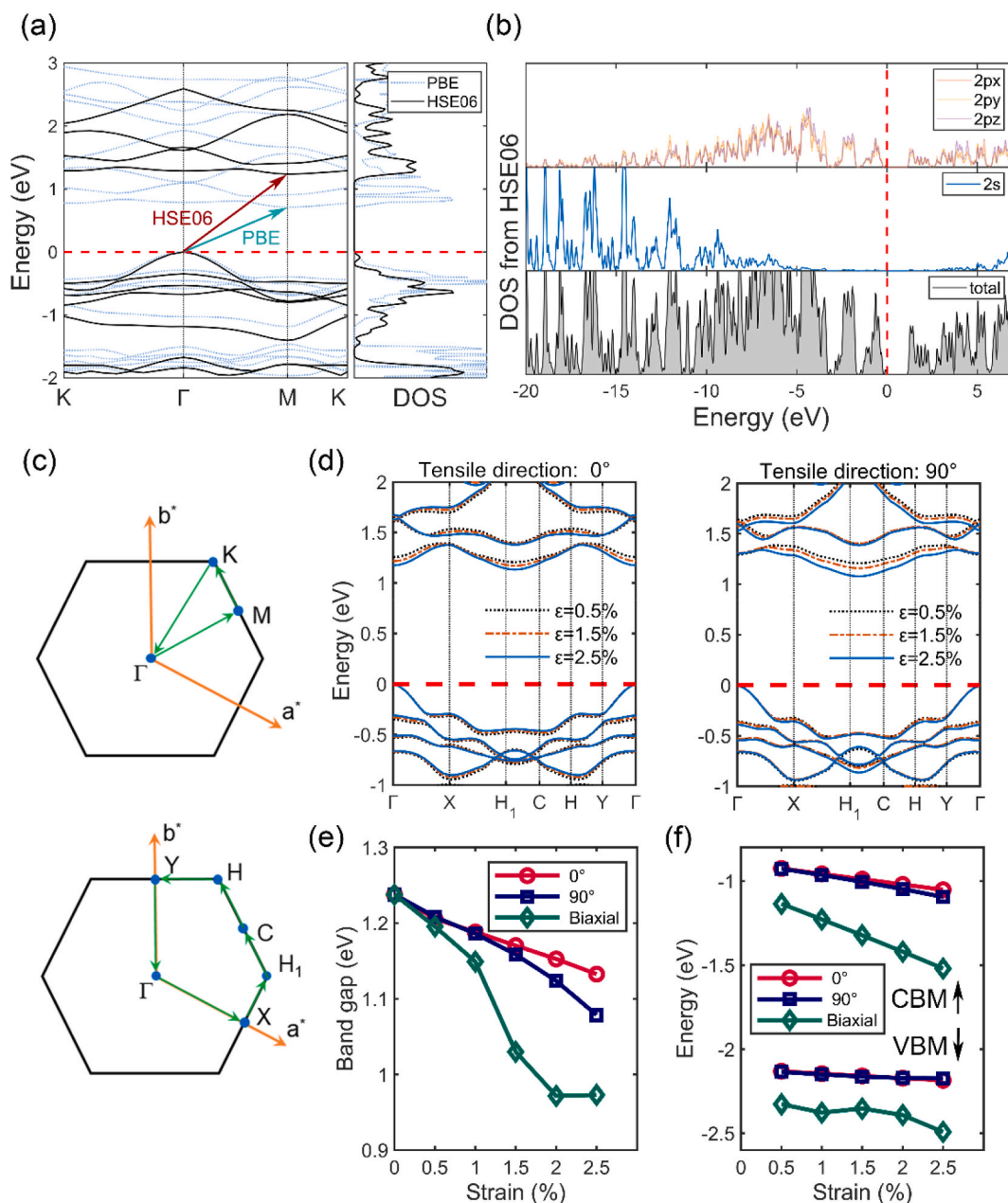Rewrite the strain tensor in matrix form,

Fig. 4. Tunable band gap in mC60 by lattice mismatch induced straining. (a) The electronic band structure (left) and DOS (right) of ground state in the vicinity of the Fermi level, calculated using PBE functional (dotted blue line) and HSE06 hybrid functional (solid black line). (b) Electronic DOS projected to 2p and 2s orbitals. (c) Brillouin zone for the structure under free and biaxial strains (upper) and those under uniaxial strains (bottom). (d) The band structure, (e) band gap and (f) frontier states under uniaxial and biaxial different tensile state at different strains using HSE06 hybrid functional. (A colour version of this figure can be viewed online.)

$$\boldsymbol{\varepsilon} = [\varepsilon_{ij}] = \begin{bmatrix} \varepsilon_1 & \gamma_{12}/2 \\ \gamma_{12}/2 & \varepsilon_2 \end{bmatrix} = A \begin{bmatrix} B_1 & B_3/2 \\ B_3/2 & B_2 \end{bmatrix} \sigma, \tag{4}$$

we obtain the nominal tensile strain ε_b in line with the bond with direction vector $\boldsymbol{n}_b$,

$$\varepsilon_b = \boldsymbol{n}_b \boldsymbol{\varepsilon} \cdot \boldsymbol{n}_b = A(B_1 cos^2\theta_b + B_2 sin^2\theta_b + B_3 \, cos \, \theta_b \, sin \, \theta_b)\sigma. \tag{5}$$

Here θ_b is the angle of a specific bond (D- or S-bonds) with respect to the loading direction, It is worth noting that for S-bonds, there may be two distinct directions.

We adopt a strain-based criterion that mC_{60} reaches its failure strength once any bond reaches its maximum tensile strain, defined as ε_d^m and ε_s^m for D-bonds and S-bonds, respectively. When D-bond failure precedes to others, the strength of mC_{60}, by inverting Eqn. (5), is

$$\sigma(\theta) = \varepsilon_d^m \, \Big/ \, \big[A(B_1 cos^2\theta + B_2 sin^2\theta - B_3 \, cos \, \theta \, sin \, \theta)\big]. \tag{6}$$

In the circumstance that S-bond breakage occurs first, mC_{60}'s strength is

$$\sigma(\theta) = \varepsilon_s^m \, \Big/ \, \Big\{A\big[B_1 cos^2(\omega-\theta) + B_2 sin^2(\omega-\theta) + B_3 \, cos(\omega-\theta)sin(\omega-\theta)\big]\Big\}. \tag{7}$$

Here ω is the direction of the two types of S-bonds. In relaxed state, it is about 65 ° and 115 °, respectively. Prior to failure, however, those angles may change due to deformation, which may give rise to slight discrepancy between theoretical predictions and DFT results. For consistence and due to the small deformation before failure, we do not rectify those strengths due to this factor. Among those values for the failure strength of D-bonds and two types of S-bonds, we always pick the lowest one for strength. Theoretical predictions on strength conditioned on failure of two types of bonds are shown in Fig. 3(c), which agrees well with DFT results. The big difference in strength between D-bonds and S-bonds are further confirmed by their respective bond energies from DFT calculations, which are 1.70 eV and 0.57 eV.

It is desired that mC_{60} may be of potential as functioning materials with its band gap close to that of silicon [40]. As mC_{60} often resides on a substrate, which may give rise to straining due to lattice mismatch, which is known to modify band gap in 2D materials [41–43]. The electronic band structure of strain-free state has been calculated using PBE functional and HSE06 hybrid functional, as shown in Fig. 4(a). The Brillouin zone and its corresponding high symmetry points are as shown in Fig. 4(c). The indirect band gap of 0.71 eV was obtained using PBE functional which systematically underestimates the band gap [44–46]. HSE06 hybrid functional [35,47] is then used which is much more precise where the Hartree-Fock method is mingled which can overestimate band gap to, thereby, cancel out the error of semi-local functional. The obtained indirect band gap using HSE06 method is 1.24 eV which is lower than the experimental reported value of 1.6 eV by ultraviolet photoemission spectroscopy (UPS) and low-energy inverse photoemission spectroscopy (LEIPS) methods [23]. It is reported that the underestimation of band gap for mC_{60} is 22.5% by HSE06 method. Except for the intrinsic systematic error of HSE06, the difference may also be contributed by the temperature effects and size effects, based on the fact that remoter atomic distance means larger band gap. Our simulations were at the ground state while the experiments are at higher temperature. In general, the moderate band gap qualifies mC_{60} with semiconducting or insulating properties.

To gain a better view of the orbital's contribution, we have studied the projected DOS of both functionals. Results from HSE06 method are shown in Fig. 4(b). The main valence bands at lower energy and part of conduction bands at higher energy are composed mainly of s components. It's clear that the outermost electrons in the p orbital, termed the valence shell, are the main contributor to band structure around the Fermi level. Three p components have almost the same contribution. The contribution from s electrons is negligible.

Strains are then applied to mC_{60} to mimic lattice mismatch. To make it practical, we focus on the strains of 'linear elastic' range. The maximum uniaxial strains of both are 2.5%, impending to the failure point but having a disturbance-tolerance. The band structures at different uniaxial strains at intervals of 0.5% along 0° and 90°, as well as biaxial strains, are studied, as shown in Fig. 4(d). The band structures exhibit strain sensitivity and similar tweaking trend respect to two directions. Those results are summarized in Fig. 4(e). There exist two kinds of descending modes congruent with two kinds of connection bonds, leading to the anisotropic tunable band gaps. We explored the behavior of frontier states with straining. In Fig. 4(f), we show how conduction band minimum (CBM) and valence band maximum (VBM) behaves with straining. From the electron location function in Fig. 2(b), we can deduce that the connection bonds play important roles in forming the band structures. The different electron location distribution and orientation of D-bonds and S-bonds are account for the anisotropy of the band gap. This tunable electronic phenomenon might be the key to full exploitation of its vast potential and guide the further fabricate of the functionalized electronic material.

4. Conclusions

In this paper, we report a systematical investigation about the anisotropy mechanical features of the newly synthesized monolayer fullerene network mC_{60} using a combination of cutting-on-edge calculations and theoretical analysis. We have examined the dynamics stabilities, structural and elastic properties, as well as tunable electronic properties. The absence of the imaginary phonon frequency justifies the dynamic stability of mC_{60}.

We then developed an analytical mechanical model to describe the unique mechanical behaviors of mC_{60} that possesses several failure modes due to the two kinds of inter-cell connection [23]. Our direction-dependent theoretical strength agrees well with the results from first-principles calculations. It is striking to see the continuum concept of bond failure works reasonably well at atomic scale when local bond strength is governed by electronic densities. It hence suggests that model could be further applied to alike anisotropic elastic brittle crystal materials and effectively predict the strength distribution without complex atomistic simulations. The tunable electronic band structures, controlled by anisotropic lattice mismatch modes along the directions of 0° and 90°, are further discussed. The obtained indirect band gap of fully relaxed structure is semiconducting with obtained indirect band gap of 1.24 eV using HSE06 method. Strain engineering could be applied to tune the band gap of mC_{60}. At a time when much carbon allotropes are realizing, the possible incorporation of the existing fascinating mC_{60} in the production of electronic devices are visible. We feel the mechanics associated with this new material may pave the road for its further exploration and possible applications, at least from the mechanical point of view.

Credit author statement

Y. Wei and Q. Peng conceived the project and proposed the dual bond model; S. Zhao, X. Zhang and Y. Wei developed the theoretical model and involved in the theoretical analysis; S. Zhao, X. Zhang and Q. Peng performed the First-principle based calculation and analysis. All authors analyzed data, discussed the results, wrote the draft, reviewed and edited the manuscript.

Declaration of competing interest

The authors declare that they have no known competing financial interests or personal relationships that could have appeared to influence the work reported in this paper.

Acknowledgment

Appendix A. Supplementary data

Supplementary data to this article can be found online at https://doi.org/10.1016/j.carbon.2022.11.005.

References

[1] S. Stankovich, D.A. Dikin, G.H. Dommett, K.M. Kohlhaas, E.J. Zimney, E.A. Stach, et al., Graphene-based composite materials, Nature 442 (7100) (2006) 282–286.

[2] T. Hu, X. Mei, Y. Wang, X. Weng, R. Liang, M. Wei, Two-dimensional nanomaterials: fascinating materials in biomedical field, Sci. Bull. 64 (22) (2019) 1707–1727.

[3] K.S. Novoselov, A.K. Geim, S.V. Morozov, D.-e. Jiang, Y. Zhang, S.V. Dubonos, et al., Electric field effect in atomically thin carbon films, Science 306 (5696) (2004) 666–669.

[4] C. Lee, X. Wei, J.W. Kysar, J. Hone, Measurement of the elastic properties and intrinsic strength of monolayer graphene, Science 321 (5887) (2008) 385–388.

[5] Y. Zhang, Y.-W. Tan, H.L. Stormer, P. Kim, Experimental observation of the quantum Hall effect and Berry's phase in graphene, Nature 438 (7065) (2005) 201–204.

[6] J.C. Meyer, A.K. Geim, M.I. Katsnelson, K.S. Novoselov, T.J. Booth, S. Roth, The structure of suspended graphene sheets, Nature 446 (7131) (2007) 60–63.

[7] A.K. Geim, Graphene: status and prospects, Science 324 (5934) (2009) 1530–1534.

[8] K.S. Novoselov, Z. Jiang, Y. Zhang, S. Morozov, H.L. Stormer, U. Zeitler, et al., Room-temperature quantum Hall effect in graphene, Science 315 (5817) (2007), 1379-1379.

[9] R.R. Nair, P. Blake, A.N. Grigorenko, K.S. Novoselov, T.J. Booth, T. Stauber, et al., Fine structure constant defines visual transparency of graphene, Science 320 (5881) (2008), 1308-1308.

[10] C. Zhang, T. Liu, A review on hybridization modification of graphene and its polymer nanocomposites, Chin. Sci. Bull. 57 (23) (2012) 3010–3021.

[11] K.S. Novoselov, L. Colombo, P. Gellert, M. Schwab, K. Kim, A roadmap for graphene, Nature 490 (7419) (2012) 192–200.

[12] K. Novoselov, Nobel lecture: graphene: materials in the flatland, Rev. Mod. Phys. 83 (3) (2011) 837.

[13] Y. Yang, Z. Song, G. Lu, Q. Zhang, B. Zhang, B. Ni, et al., Intrinsic toughening and stable crack propagation in hexagonal boron nitride, Nature 594 (7861) (2021) 57–61.

[14] J. Deng, B. Xia, X. Ma, H. Chen, H. Shan, X. Zhai, et al., Epitaxial growth of ultraflat stanene with topological band inversion, Nat. Mater. 17 (12) (2018) 1081–1086.

[15] M.C. Chang, P.H. Ho, M.F. Tseng, F.Y. Lin, C.H. Hou, I.K. Lin, et al., Fast growth of large-grain and continuous MoS2 films through a self-capping vapor-liquid-solid method, Nat. Commun. 11 (1) (2020) 3682.

[16] C. YanHuan, L. HuiBiao, L. YuLiang, Progress and prospect of two dimensional carbon graphdiyne, Chin. Sci. Bull. 61 (26) (2016) 2901–2912.

[17] Y. Hu, C. Wu, Q. Pan, Y. Jin, R. Lyu, V. Martinez, et al., Synthesis of γ-graphyne using dynamic covalent chemistry, Nature Synthesis (2022) 1–6.

[18] C.T. Toh, H. Zhang, J. Lin, A.S. Mayorov, Y.P. Wang, C.M. Orofeo, et al., Synthesis and properties of free-standing monolayer amorphous carbon, Nature 577 (7789) (2020) 199–203.

[19] C. Sun, B. Wen, B. Bai, Recent advances in nanoporous graphene membrane for gas separation and water purification, Sci. Bull. 60 (21) (2015) 1807–1823.

[20] Q.H. Wang, K. Kalantar-Zadeh, A. Kis, J.N. Coleman, M.S. Strano, Electronics and optoelectronics of two-dimensional transition metal dichalcogenides, Nat. Nanotechnol. 7 (11) (2012) 699–712.

[21] J. Wilson, F. Di Salvo, S. Mahajan, Charge-density waves in metallic, layered, transition-metal dichalcogenides, Phys. Rev. Lett. 32 (16) (1974) 882.

[22] J.N. Coleman, M. Lotya, A. O'Neill, S.D. Bergin, P.J. King, U. Khan, et al., Two-dimensional nanosheets produced by liquid exfoliation of layered materials, Science 331 (6017) (2011) 568–571.

[23] L. Hou, X. Cui, B. Guan, S. Wang, R. Li, Y. Liu, et al., Synthesis of a monolayer fullerene network, Nature 606 (7914) (2022) 507–510.

[24] Y. Wei, J. Wu, H. Yin, X. Shi, R. Yang, M. Dresselhaus, The nature of strength enhancement and weakening by pentagon–heptagon defects in graphene, Nat. Mater. 11 (9) (2012) 759–763.

[25] I.I. Alahmed, S.M. Altanany, I. Abdulazeez, H. Shoaib, A.Q. Alsayoud, A. Abbout, et al., The crack angle of 60° is the most vulnerable crack front in graphene according to MD simulations, Crystals 11 (11) (2021) 1355.

[26] H. Yin, H.J. Qi, F. Fan, T. Zhu, B. Wang, Y. Wei, Griffith criterion for brittle fracture in graphene, Nano Lett. 15 (3) (2015) 1918–1924.

[27] Z. Pang, X. Gu, Y. Wei, R. Yang, M.S. Dresselhaus, Bottom-up design of three-dimensional carbon-honeycomb with superb specific strength and high thermal conductivity, Nano Lett. 17 (1) (2017) 179–185.

[28] R.M. Tromer, L.A.R. Junior, D.S. Galvão, A DFT study of the electronic, optical, and mechanical properties of a recently synthesized monolayer fullerene network, Chem. Phys. Lett. (2022), 139925.

[29] G. Kresse, J. Furthmüller, Efficient iterative schemes for ab initio total-energy calculations using a plane-wave basis set, Phys. Rev. B 54 (16) (1996), 11169.

[30] P.E. Blöchl, Projector augmented-wave method, Phys. Rev. B 50 (24) (1994), 17953.

[31] J.P. Perdew, K. Burke, M. Ernzerhof, Generalized gradient approximation made simple, Phys. Rev. Lett. 77 (18) (1996) 3865.

[32] H.J. Monkhorst, J.D. Pack, Special points for Brillouin-zone integrations, Phys. Rev. B 13 (12) (1976) 5188.

[33] S. Grimme, J. Antony, S. Ehrlich, H. Krieg, A consistent and accurate ab initio parametrization of density functional dispersion correction (DFT-D) for the 94 elements H-Pu, J. Chem. Phys. 132 (15) (2010) 154104.

[34] X. Gu, R. Yang, First-principles prediction of phononic thermal conductivity of silicene: a comparison with graphene, J. Appl. Phys. 117 (2) (2015), 025102.

[35] A.V. Krukau, O.A. Vydrov, A.F. Izmaylov, G.E. Scuseria, Influence of the exchange screening parameter on the performance of screened hybrid functionals, J. Chem. Phys. 125 (22) (2006), 224106.

[36] A. Togo, I. Tanaka, First principles phonon calculations in materials science, Scripta Mater. 108 (2015) 1–5.

[37] H. Yu, L.-C. Chen, H.-J. Pang, P.-F. Qiu, Q. Peng, X.-J. Chen, Temperature-dependent phonon anharmonicity and thermal transport in CuInTe 2, Phys. Rev. B 105 (24) (2022), 245204.

[38] M. Maździarz, Comment on 'The Computational 2D Materials Database: high-throughput modeling and discovery of atomically thin crystals, 2D Mater. 6 (4) (2019), 048001.

[39] S.J. Stuart, A.B. Tutein, J.A. Harrison, A reactive potential for hydrocarbons with intermolecular interactions, J. Chem. Phys. 112 (14) (2000) 6472–6486.

[40] b.H. Morkoc, S. Strite, G. Gao, M. Lin, B. Sverdlov, M. Burns, Large-band-gap SiC, III-V nitride, and II-VI ZnSe-based semiconductor device technologies, J. Appl. Phys. 76 (3) (1994) 1363–1398.

[41] Y. Lu, J. Guo, Local strain in tunneling transistors based on graphene nanoribbons, Appl. Phys. Lett. 97 (7) (2010), 073105.

[42] C. Lin, M. Ochi, R. Noguchi, K. Kuroda, M. Sakoda, A. Nomura, et al., Visualization of the strain-induced topological phase transition in a quasi-one-dimensional superconductor TaSe3, Nat. Mater. 20 (8) (2021) 1093–1099.

[43] L. Zhang, W. Geng, C.-j. Tong, X. Chen, T. Cao, M. Chen, Strain induced electronic structure variation in methyl-ammonium lead iodide perovskite, Sci. Rep. 8 (1) (2018) 1–9.

[44] J.P. Perdew, M. Levy, Physical content of the exact Kohn-Sham orbital energies: band gaps and derivative discontinuities, Phys. Rev. Lett. 51 (20) (1983) 1884.

[45] P. Mori-Sánchez, A.J. Cohen, W. Yang, Localization and delocalization errors in density functional theory and implications for band-gap prediction, Phys. Rev. Lett. 100 (14) (2008), 146401.

[46] J.M. Crowley, J. Tahir-Kheli, W.A. Goddard III, Resolution of the band gap prediction problem for materials design, J. Phys. Chem. Lett. 7 (7) (2016) 1198–1203.

[47] P. Deák, B. Aradi, T. Frauenheim, E. Janzén, A. Gali, Accurate defect levels obtained from the HSE06 range-separated hybrid functional, Phys. Rev. B 81 (15) (2010), 153203.